

# On the origin of compressive turbulence in protoclumps in high redshift disks

Omry Ginzburg<sup>1</sup>, Avishai Dekel<sup>1,2</sup>, Nir Mandelker<sup>1</sup>, Frederic Bournaud<sup>3</sup>, Daniel Ceverino<sup>4,5</sup>, and Joel Primack<sup>6</sup>

<sup>1</sup> Racah Institute of Physics, The Hebrew University, Jerusalem 91904 Israel

<sup>2</sup> SCIPP, University of California, Santa Cruz, CA 95064, USA

<sup>3</sup> AIM, CEA, CNRS, Université Paris-Saclay, Université Paris Diderot, Sorbonne Paris Cité, 91191 Gif-sur-Yvette, France

<sup>4</sup> Departamento de Física Teórica, Modulo 8, Facultad de Ciencias, Universidad Autónoma de Madrid, 28049 Madrid, Spain

<sup>5</sup> CIAFF, Facultad de Ciencias, Universidad Autónoma de Madrid, 28049 Madrid, Spain

<sup>6</sup> Department of Physics, University of California, Santa Cruz, CA, 95064, USA

Received -; accepted -

## ABSTRACT

*Context.* The giant, star forming clumps in gas-rich, high redshift disks are commonly assumed to form due to gravitational instabilities, in which protoclumps have a Toomre- $Q$  parameter less than unity. However, some cosmological simulations have shown that clumps can form in regions where  $Q$  is significantly greater than unity. In these simulations, there is an energy excess of compressive modes of turbulence that lead to gravitational collapse of regions that were not supposed to collapse under their own self-gravity, according to linear Toomre instability. In contrast, sites of clump formation in isolated simulations do not show this excess, hinting that the origin of the compressive turbulence is external.

*Aims.* We explore two external mechanisms that can induce the compressive modes of disk turbulence in protoclumps, namely, compressive tides exerted by the cosmological environment and the direct driving by inflowing streams.

*Methods.* We correlate the local strength of compressive tides and the amount of fresh stream material with protoclump regions in zoom-in cosmological simulations. The local strength of compressive tides is derived from the eigenvalues of the tidal tensor. The local strength of incoming streams is derived from the fractional presence of the stream compared to the average.

*Results.* We find that the tidal field in protoclumps tends to be over-compressive while random patches in the disk show substantial diverging tides. In particular, in 25% of the protoclumps, the tidal field is fully compressive, while no random patch resides in regions of fully compressive tides. In addition, the protoclumps tend to reside in regions where the fraction of incoming stream mass is 2-10 times larger than the average at the same galactocentric radius.

*Conclusions.* Both compressive tides and inflowing streams are correlated with the protoclumps and can thus serve as the drivers of excessive compressive turbulence that can initiate clump formation before self-gravity takes over. This constitutes a new, non-linear mode of violent disk instabilities in high- $z$  galaxies.

**Key words.** ISM: Kinematics and dynamics – ISM: Structure – Galaxies: formation – Galaxies: high-redshift

## 1. Introduction

High-redshift galactic disks are observed to be highly perturbed, sustaining supersonic levels of turbulence (Hennebelle & Falgarone 2012; Kassin et al. 2012; Rowland et al. 2024), and hosting giant, kiloparsec-scale clumps (Genzel et al. 2008; Guo et al. 2018; Zanella et al. 2019; Fujimoto et al. 2024). Approximately 40 – 60% of galaxies in the redshift range  $1 \leq z \leq 4$  appear to exhibit such clumpy structures (Guo et al. 2015; Shibuya et al. 2016). These clumps are prominent across various wavelengths, appearing in rest-frame UV (Wuyts et al. 2012; Guo et al. 2015; Sattari et al. 2023), H $\alpha$  emission (Genzel et al. 2011; Swinbank et al. 2012; Livermore et al. 2015), CII (Zanella et al. 2024), as well as rest-frame optical and IR (Förster Schreiber et al. 2011; Kalita et al. 2024). They contribute roughly 10 – 20% of the galaxy’s total star formation rate (SFR), while their observed masses are more uncertain due to the limited resolution (Cava et al. 2018; Meng & Gnedin 2020; Huertas-Company et al. 2020).

The presence of clumps in galactic disks significantly influences their structural and dynamical evolution. Clumps are

believed to play a pivotal role in radial mass transport within the disk (Dekel et al. 2009; Dekel & Burkert 2014; Genzel et al. 2023; cf. Dutta Chowdhury et al. 2024), in contributing to bulge growth (Zolotov et al. 2015; Lapiner et al. 2023); in creating cored dark matter halos through dynamical friction heating (Ogiya & Nagai 2022); and in driving turbulence via clump-clump and clump-disk interactions (Dekel et al. 2009; Krumholz & Burkert 2010). These processes are relevant if clumps persist long enough to participate in them. Clump longevity remains under debate, with some studies suggesting a substantial fraction of long-lived clumps (Mandelker et al. 2017) and others arguing for a prolonged clumpy phase composed of short-lived clumps (Oklopčić et al. 2017). Disk properties, such as gas fraction, contribute to clump longevity (Renaud et al. 2024), but stellar and supernova feedback are likely the primary factors. Thus, clumps hold critical insights into feedback processes in galaxies (Mayer et al. 2016; Ceverino et al. 2023; Dekel et al. 2022; cf. Fensch & Bournaud 2020), helping to constrain them.

Observationally, clump age gradients support the existence of long-lived clumps and their migration toward the galactic center (Shibuya et al. 2016; Guo et al. 2018). In Ginzburg et al.

(2021), we applied deep learning techniques to identify clumps in star-forming galaxies from the CANDELS survey, and classify them by longevity (short- or long-lived), based on cosmological simulations of clumpy galaxies (Mandelker et al. 2017). Our findings indicated that these galaxies host long-lived clumps that tend to migrate inward. Theoretically, analytical models of clump survival and migration suggest that clumps in gas-rich galaxies with stellar masses around  $M_* \sim 10^{9.3} M_\odot$  at  $z \sim 2$  are likely to survive and migrate, typically reaching the center within  $\sim 10$  clump free-fall times (Dekel et al. 2022). Cosmological simulations, however, present a more complex picture. While the VELA3 simulations (Ceverino et al. 2014; Zolotov et al. 2015; Mandelker et al. 2017) clearly indicate the presence of long-lived clumps, the VELA6 simulations (Ceverino et al. 2023), as well as the FIRE simulations (Oklopčić et al. 2017) predominantly show short-lived clumps. The FIRE simulations typically exhibit outflow mass-loading factors  $\eta \equiv \dot{M}_{\text{out}}/\text{SFR} \sim 4 - 10$  and outflow velocities of  $400 - 700 \text{ km s}^{-1}$  (Muratov et al. 2015) in the relevant mass and redshift range. In contrast, for massive, long-lived clumps in VELA (as seen in Fig. 13 of Mandelker et al. (2017)), the mass-loading factor is around unity or less. This mass-loading factor is consistent with observational estimate for ionized gas outflows driven by stellar and supernova feedback (Förster Schreiber et al. 2019).

While the giant clumps could have formed ex situ, being the remnants of small galaxies that merged with the disk, it is believed that most clumps are formed in situ, due to local gravitational collapse. The common understanding of in situ clump formation is that they arise from violent disk instability, governed by the Toomre instability (Toomre 1964). In this picture, a razor thin disk becomes linearly unstable to axisymmetric perturbations when  $Q \equiv \kappa\sigma/\pi G\Sigma < 1$ . Here,  $\kappa$  is the epicyclic frequency,  $\sigma$  is the radial velocity dispersion (either thermal or turbulent), and  $\Sigma$  is the surface density. While it is convenient and quite common to evaluate the  $Q$  parameter using global values of the disk, the  $Q$  parameter is derived locally, at each galactocentric radius, by assuming the scales of the perturbations are much smaller than the disk scale radius (Binney & Tremaine 2008).

Disks are typically assumed to be in a state of “marginal instability” where  $Q \sim 1$ . This is based on the following qualitative argument (Noguchi 1999; Dekel et al. 2009): if a disk’s  $Q$  drops below unity, the disk starts to fragment into rings in the linear regime, which later fragment non-linearly into clumps, thus developing non-axisymmetric features in the disk. Star formation within these clumps induces strong stellar feedback, and torques due to the non-axisymmetric features drive angular momentum outward and thus mass inward, which flows down the potential well towards a central bulge. Both stellar feedback and radial mass transport are sources of turbulence (Krumholz et al. 2018), which raises the velocity dispersion and consequently  $Q$  above unity. When  $Q$  grows above unity, the disk stabilizes, clumps and non-axisymmetric features diminish, and turbulence-driving mechanisms weaken, allowing  $\sigma$  to decrease and  $Q$  to eventually fall below unity again. This cyclical regulation maintains the disk in a state of marginal stability, with  $Q \sim 1$ . This was confirmed in numerical simulations of isolated disks (Bournaud & Elmegreen 2009; Immeli et al. 2004; Hopkins et al. 2012), as well as observations (Genzel et al. 2014; Fisher et al. 2017). However, caution should be taken when measuring  $Q$  in observations, especially in clumps, because these measurements are usually dominated by the high surface density, non linear structures, where  $Q$  is no longer meaningful.

In a cosmological setting, however, the situation is more complex. Inoue et al. (2016) showed that, in the VELA simulations, clumps are formed out of ‘protoclump’ regions, where the local  $Q$  parameter is greater than unity, and occasionally substantially greater. This calls into question the validity of the local linear Toomre analysis in cosmological disks. Several other formation mechanisms for clumps are possible. For example, Inoue & Yoshida (2018) suggest a two stage formation of clumps, beginning with the development of spiral arms when  $Q \sim 2$ , followed by the fragmentation of these arms to clumps when  $Q \sim 0.6$ . However, this does not explain the clump formation in regions with  $Q > 3$  in VELA. Another possibility is the rapid dissipation of turbulence in perturbed regions. Elmegreen (2011) showed that if significant energy dissipation occurs within a crossing time, the threshold for stability increases to  $Q \sim 2 - 3$ , again insufficient to explain the clump formation found by Inoue et al. (2016). Lovelace & Hohlfield (1978) derived a *necessary* condition for non-axisymmetric perturbations to be unstable based on the existence of a local extremum of  $f(r) = \Sigma\Omega/\kappa^2$ . Some galaxies in the VELA simulations did show such a local extremum (Inoue et al. 2016), so it is possible that some clumps are formed due to non-axisymmetric perturbations. Other theories (e.g. Griv & Gedalin 2012) eventually boil down to a stability criterion of  $Q \gtrsim 2$ .

In Mandelker et al. (2024) (henceforth M24), we initiated the exploration of the possibility that clumps form out of protoclump regions with high levels of compressive turbulence. Broadly speaking, the turbulence velocity field can be thought of as composed of a compressive part, representing the local tendency to converge to or diverge from a point, and a solenoidal part, representing the local tendency to rotate about a point. In a steady state, isotropic and homogeneous turbulent field in equipartition, the global ratio of energy in compressive modes to total turbulent energy is  $\sim 1/3$ . However, if for any reason there is a deviation from this value in favor of compressive modes, the turbulence itself is able to generate more dense regions (Padoan & Nordlund 2002; Federrath et al. 2010), that can be sufficient for self gravity to take over, while having large velocity dispersions that keep  $Q$  above unity. Indeed, Hopkins & Christiansen (2013) found that, statistically,  $Q$  parameters of  $\gtrsim 5^1$  are marginally stable in highly supersonic disks.

While inspecting both cosmological and isolated simulations, M24 found that protoclump regions in cosmological simulations do show an excess of energy in compressive modes, while protoclump regions in isolated simulations do not. It thus implies that the cosmological environment drives more compressive turbulence by physical processes that are absent in an isolated setting. In this work, we examine two possible causes for the excess of compressive modes of turbulence in a cosmological environment: compressive gravitational tides and stream-disk interaction. For the former, several studies showed that during galaxy mergers or other strong interactions, elevated levels of compressive tides induces clump and cluster formations, as well as high levels of compressive turbulence (Renaud et al. 2009, 2014, 2022; Li et al. 2022). Mergers can also induce clump formation by the wake they produce during the merger (Nakazato et al. 2024). For the latter, stream-disk interaction has the poten-

<sup>1</sup> Hopkins & Christiansen (2013) found that for highly supersonic turbulence, a disk is never *statistically* stable. Their study focused on protoplanetary disks. However, adopting model parameters suited to galactic disks, where turbulence is driven by multiple mechanisms with significant morphological variations, suggests a more appropriate  $Q$  threshold of  $\sim 5$ .

tial to drive turbulence due to the collisions between the flows (see discussion in §4.2).

The paper is organized as follows. In §2 we introduce the methods used in the analysis, including the turbulence decomposition (§2.3), the tidal field analysis (§2.4) and the stream-disk interaction analysis (§2.5). In §3 we present our main analysis - in §3.2 we present a comparison the fraction of energy in compressive modes, the tides and the presence of streams between protoclumps and random patches, and in §3.3 we correlate the different quantities. In §4 we discuss some caveats, and in §5 we present our conclusions.

## 2. Methods

### 2.1. The VELA cosmological simulations

We analyze eight galaxies from the VELA3 suite of cosmological simulations<sup>2</sup> (Ceverino et al. 2014; Mandelker et al. 2017). The simulations use the ART code (Kravtsov et al. 1997; Ceverino & Klypin 2009), which is a gravito-hydrodynamics, grid-based, adaptive mesh refinement code, with a maximal resolution of  $\sim 17 - 35$  proper pc at all times, down to  $z \sim 1$ . The dark matter mass resolution is  $8.3 \cdot 10^4 M_\odot$ , and the minimal stellar particle mass is  $10^3 M_\odot$ . The code includes gas and metal cooling, UV-background photoionization and self shielding in dense gas, stochastic star-formation, thermal feedback, radiation pressure and metal enrichment from stellar feedback (Ceverino et al. 2010, 2012, 2014). A more detailed description of the simulations can be found in Ceverino et al. (2014) and Mandelker et al. (2017). We use the high temporal resolution version of the simulations, which has  $\sim 30$  snapshots per disc orbital time.

All of the eight galaxies undergo a phase of compaction to a blue nugget (sometimes multiple; Zolotov et al. 2015; Lapiner et al. 2023), which involves a rapid increase in the central gas density, followed by an intense starburst and subsequent inside-out quenching. These compaction events are usually triggered by a major merger (Lapiner et al. 2023), although not exclusively. The galactic disk survives for long periods of time when the halo mass exceeds  $\sim 10^{11} M_\odot$  (Dekel et al. 2020), which typically occurs after the compaction event. Thus, the main violent, disk<sup>3</sup> phase of the galaxies typically lasts from  $z \sim 4 - 1$  (Mandelker et al. 2017; Dekel et al. 2022), which is roughly the period of time analyzed in Inoue et al. (2016) and M24.

### 2.2. Clump finder & protoclumps

We use the clump finder developed by Mandelker et al. (2017). In short, the 3D density field of baryons is dumped onto a uniform grid with grid spacing of  $\Delta x = 70$ pc. The grid is then smoothed with a spherical Gaussian with full-width-at-half-maximum of  $W = 2.5$ kpc. The residual,  $\delta$ , is then defined as  $\delta = (\rho - \rho_w)/\rho$ , where  $\rho$  and  $\rho_w$  are the raw and smoothed density fields, respectively. Clumps are defined as connected regions containing at least eight uni-grid cells with  $\delta > 10$ , as defined using either stellar density, or the combined density of cold gas ( $T < 1.5 \cdot 10^4$  K) and young stars (stellar age  $< 100$  Myr).

<sup>2</sup> The galaxies we analyze are labeled V07, V08, V11, V12, V14, V25, V26 and V27, in accordance with table 1 in Mandelker et al. (2017).

<sup>3</sup> The galactic disk's dimensions and orientation are defined by those of the cylinder that contains 85% of the cold component, consisting of gas with  $T < 10^4$  K and young stars with age  $< 100$  Myr, within  $0.15R_{\text{vir}}$  (Mandelker et al. 2017).

Since VELA uses ART, which is a grid-based code, and the current run did not include tracer particles, clumps are tracked through time based on their stellar particles. We only track clumps that contain at least ten stellar particles. For each such clump at a given snapshot, we search for all clumps in the previous snapshot that contribute at least 25% of their stellar particles to the current clump. If a given clump has more than one such progenitor, we consider the most massive one as the main progenitor, and the others as having merged with it. The formation time of the clump is considered to be the snapshot at which no progenitor was found in the two preceding snapshots. The clumps in VELA were studied in detail in Mandelker et al. (2017), and their properties are consistent with properties of observed clumps (Guo et al. 2018; Ginzburg et al. 2021).

To define protoclump regions, i.e. the regions out of which clumps form, we take the center-of-mass velocity of the clump at its initial formation snapshot in cylindrical coordinates  $(v_r, v_\phi, v_z)$ , and extrapolate the position one snapshot back in time to determine the position of the protoclump. Assuming that the clump has just formed, and given the high temporal resolution, it is safe to assume that the clump's velocity is still attached to the overall disk velocity field. For the size of the protoclumps, since most of the collapsed clumps have radii in the range  $R_C \sim 100 - 300$ pc (Mandelker et al. 2017), and clumps usually contract by a factor of two to three (Ceverino et al. 2012; Dekel et al. 2023), we use a fixed radius of  $R_{\text{PC}} = 0.5$  kpc for all protoclumps. We tested our results for  $R_{\text{PC}} = 0.8$  kpc with no qualitative difference.

### 2.3. Turbulence decomposition

The heart of our analysis is based on compressive turbulence. Compressible turbulence in general, and compressive turbulence in particular<sup>4</sup> has been shown to impact the density distribution of interstellar gas (Federrath et al. 2010), which in turn affects star formation in regions with excess of compressive turbulence.

While compressive turbulence is conceptually simple to understand, it is mathematically more challenging to define. Below, we give two definitions, one local and one global, each having advantages but also drawbacks that present a caveat in our analysis. Discussion of these caveats is present in §4.3.

A word on terminology - we call the mode of turbulence that describes a tendency to locally diverge or converge to a point the 'compressive mode', and the mode of turbulence that describes a tendency to locally rotate about a point the 'solenoidal mode'. Out of the two possible directions of the compressive mode, we have the 'converging mode', for which  $\nabla \cdot \mathbf{v} < 0$ , and the 'diverging mode', for which  $\nabla \cdot \mathbf{v} > 0$ .

#### 2.3.1. Global decomposition

Every vector field  $\mathbf{v}(\mathbf{r})$  can be decomposed, using the Helmholtz decomposition, to curl-free, divergence-free and harmonic components

$$\mathbf{v}(\mathbf{r}) = \nabla\phi + \nabla \times \mathbf{A} + \nabla\psi \equiv \mathbf{v}_{\text{comp}} + \mathbf{v}_{\text{sol}} + \mathbf{v}_{\text{har}}, \quad (1)$$

where  $\phi, \psi$  are scalar functions, with  $\psi$  satisfying  $\nabla^2\psi = 0$  and  $\mathbf{A}$  is a vector function. In order to perform this decomposition, ap-

<sup>4</sup> The former is the more general notion of allowing supersonic flows and shocks, while the latter generally refers to the tendency of the velocity field to converge to a point.



appropriate boundary conditions are needed. Two types boundary conditions are commonly assumed, which make the decomposition straightforward - vanishing at infinity or periodic - both of which are not applicable in the local case. For the former,  $\mathbf{v} \rightarrow 0$  as  $|\mathbf{r}| \rightarrow \infty$ , then necessarily  $\psi = \text{const}$  since  $\psi$  solves Laplace's equation with  $\nabla\psi = 0$  at the boundary<sup>5</sup>. The value of  $\psi$  is not physically important, only its gradient, which is zero. For the latter type of boundary condition, in a periodic box,  $\psi = 0$ , since a harmonic function cannot be periodic in every direction, and if  $\mathbf{v}$  is periodic,  $\nabla\psi$  must be periodic, hence  $\psi$  must be periodic.

In either of these cases, a periodic box or an infinite domain where  $\mathbf{v} \rightarrow 0$  as  $|\mathbf{r}| \rightarrow \infty$ , the decomposition can be performed using the Fourier transform. This is achieved by projecting the Fourier transform of the velocity field along the wavevector  $\mathbf{k}$  and perpendicular to  $\mathbf{k}$ ,

$$G_\phi(\mathbf{k}) = \frac{i\mathbf{k} \cdot \tilde{\mathbf{v}}}{|\mathbf{k}|^2}, \quad G_A(\mathbf{k}) = \frac{i\mathbf{k} \times \tilde{\mathbf{v}}}{|\mathbf{k}|^2}.$$

Here,  $\tilde{\mathbf{v}}$  is the Fourier transform of  $\mathbf{v}$ . Using these two functions, we can write the Fourier transform of  $\mathbf{v}$  as

$$\tilde{\mathbf{v}} = -i\mathbf{k}G_\phi + i\mathbf{k} \times G_A. \quad (2)$$

The desired curl-free and divergence-free parts are determined by the inverse Fourier transform of the above two terms. It is evident from this decomposition that  $\nabla \cdot \mathbf{v}_{\text{comp}} = \nabla \cdot \mathbf{v}$  and  $\nabla \times \mathbf{v}_{\text{sol}} = \nabla \times \mathbf{v}$ .

From Parseval's theorem, one finds that  $\mathbf{v}_{\text{comp}}$  and  $\mathbf{v}_{\text{sol}}$  are orthogonal in the global sense, i.e.

$$\int |\mathbf{v}|^2 d^3\mathbf{r} = \int |\mathbf{v}_{\text{comp}}|^2 d^3\mathbf{r} + \int |\mathbf{v}_{\text{sol}}|^2 d^3\mathbf{r}, \quad (3)$$

but **not** in a local sense (i.e.,  $\mathbf{v}_{\text{comp}} \cdot \mathbf{v}_{\text{sol}} \neq 0$ ). This can easily be understood from the uncertainty principle - the decomposition is locally orthogonal in  $\mathbf{k}$ -space, and therefore only globally orthogonal in  $\mathbf{r}$ -space<sup>6</sup>. Another caveat with this decomposition is that it is possible to construct a velocity field such that at a given point,  $\mathbf{r}_0$ ,  $\mathbf{v}(\mathbf{r}_0) = 0$ , while  $\mathbf{v}_{\text{comp}}(\mathbf{r}_0)$ ,  $\mathbf{v}_{\text{sol}}(\mathbf{r}_0) \neq 0$ . Thus, assuming that  $|\mathbf{v}_{\text{comp}}|^2$  and  $|\mathbf{v}_{\text{sol}}|^2$  represent some local energy densities in a region, even if relatively isolated, can introduce significant errors.

Nevertheless, we can use this decomposition to robustly define the global fraction of energy in compressive modes of turbulence (see also Federrath et al. 2010; Brunt & Federrath 2014), that is

$$f_{\text{comp, glob}} = \frac{\int |\mathbf{v}_{\text{comp}}|^2 d^3\mathbf{r}}{\int |\mathbf{v}|^2 d^3\mathbf{r}}. \quad (4)$$

While it can be analytically proven, it is intuitive to understand that in a fully isotropic and homogeneous turbulence in equipartition,  $f_{\text{comp, glob}} = 1/3$  - converging or diverging to or from a

<sup>5</sup> Suppose  $\nabla\psi = 0$  on the boundary. Let  $D_0$  be some arbitrarily chosen point on the boundary. Then, if  $D$  is any point on the boundary,  $\psi(D) - \psi(D_0) = \int \nabla\psi \cdot d\mathbf{l} = 0$ , where the integration is along the boundary. This shows that  $\psi(D) = \psi(D_0)$  for all points  $D$  on the boundary. Thus,  $\psi$  solves the Laplace equation with  $\psi = \text{const}$ . on the boundary. From the uniqueness theorem for Laplace's equation,  $\psi = \text{const}$ . in the entire volume.

<sup>6</sup> We have that  $|\mathbf{v}|^2 = |\mathbf{v}_{\text{comp}}|^2 + |\mathbf{v}_{\text{sol}}|^2 + 2\mathbf{v}_{\text{comp}} \cdot \mathbf{v}_{\text{sol}}$ , where the last term is, in general, not zero.

point is a one dimensional radial motion, while rotation (characterized by the solenoidal mode) about a point is two dimensional. Furthermore, for a fully isotropic and homogeneous turbulence in equipartition, the converging mode is half the total compressive power.

### 2.3.2. Local decomposition

Given the inherit non-locality of the Helmholtz decomposition, a different method is required to characterize the compressiveness of the turbulence field on small, protoclump scales. The most common approach is based on the following. If  $\mathbf{v}$  is a velocity field, then Taylor expanding to linear order about a point  $\mathbf{r}$  results in

$$\mathbf{v}(\mathbf{r} + \delta\mathbf{r}) \approx \mathbf{v} + \frac{1}{3}(\nabla \cdot \mathbf{v})\delta\mathbf{r} + \frac{1}{2}\boldsymbol{\omega} \times \delta\mathbf{r} + \overleftrightarrow{S} \delta\mathbf{r}, \quad (5)$$

where  $\boldsymbol{\omega} = \nabla \times \mathbf{v}$  is the vorticity, and  $\overleftrightarrow{S}$  is a traceless symmetric tensor representing shearing motion. While the second and third terms in eq. 5 are orthogonal, the shear term is, in general, not orthogonal to either of them. This raises a complication in interpreting each component individually as a contributor to the total energy in the turbulence field.

Other works tend to neglect the shearing term (Kida & Orszag 1990; Kritsuk et al. 2007; Renaud et al. 2014), and then the total turbulent kinetic energy in a sphere of radius  $R$  is

$$E_K \approx \frac{1}{9}(\nabla \cdot \mathbf{v})^2 \int r^4 d^3\mathbf{r} + \frac{1}{4}|\nabla \times \mathbf{v}|^2 \int r^4 \sin^2 \theta d^3\mathbf{r}, \quad (6)$$

where the factor of  $\sin^2 \theta$  comes from the cross product between  $\boldsymbol{\omega}$  and  $\mathbf{r}$ . After integrating, we get

$$E_K \approx \frac{4\pi R^5}{9}(\nabla \cdot \mathbf{v})^2 + \frac{2\pi}{3}|\nabla \times \mathbf{v}|^2 \frac{R^5}{5}. \quad (7)$$

This motivates defining  $|\nabla \cdot \mathbf{v}|^2$  as the local energy in compressive modes<sup>7</sup>, and  $|\nabla \times \mathbf{v}|^2$  as the local energy in solenoidal modes<sup>8</sup>. We take the same approach, and discuss its caveats and potential future directions in §4.3. We thus define the local fraction of energy in converging mode, at a given point, as

$$f_{\text{conv, loc}} = \frac{|\nabla \cdot \mathbf{v}|_{\text{neg}}^2}{|\nabla \cdot \mathbf{v}|^2 + |\nabla \times \mathbf{v}|^2}, \quad (8)$$

where  $|\nabla \cdot \mathbf{v}|_{\text{neg}}^2$  refers to regions with negative divergence, representing compression (as opposed to expansion). For a given region, the total fraction of energy in converging modes is thus

$$f_{\text{conv}} = \frac{\int |\nabla \cdot \mathbf{v}|_{\text{neg}}^2 d^3\mathbf{r}}{\int |\nabla \cdot \mathbf{v}|^2 d^3\mathbf{r} + \int |\nabla \times \mathbf{v}|^2 d^3\mathbf{r}}. \quad (9)$$

In Appendix A, we show that for a turbulent field in which the power spectrum of  $\mathbf{v}_{\text{comp}}$  and  $\mathbf{v}_{\text{sol}}$  are proportional, with the appropriate boundary conditions, when integrating over the entire

<sup>7</sup> The divergence part is smaller than the curl part by a factor of 2/3. This amounts to a factor of  $\sim 0.8$  in the local fraction as defined in eq. 9, which doesn't affect the qualitative results.

<sup>8</sup> Other possible reasonings behind this definition are either the correspondence with the Helmholtz decomposition, eq. 10, or from the fact that the viscous dissipation rate can be decomposed to a solenoidal and compressive part, as shown in Appendix B. Both of these explanations rely on specific boundary conditions.

volume,

$$\frac{\int |v_{\text{comp}}|^2 d^3\mathbf{r}}{\int |v|^2 d^3\mathbf{r}} = \frac{\int |\nabla \cdot \mathbf{v}|^2 d^3\mathbf{r}}{\int |\nabla \cdot \mathbf{v}|^2 d^3\mathbf{r} + \int |\nabla \times \mathbf{v}|^2 d^3\mathbf{r}}. \quad (10)$$

Thus, the definitions of eq. 9 and 4 agree, contingent on the appropriate boundary conditions.

To calculate the local fraction in our simulations, we follow the method of M24. First, we dump our AMR grid onto a uniform grid with 0.2 kpc resolution. Then, we compute the nine derivatives of the velocity field,  $\partial v_i / \partial r_j$ , using a second order, centered finite differences method. Then, for a given region, we integrate over its volume the quantities  $|\nabla \cdot \mathbf{v}|_{\text{neg}}^2$  (taking into account only cells with negative divergence),  $|\nabla \cdot \mathbf{v}|^2$  and  $|\nabla \times \mathbf{v}|^2$ . We then define  $f_{\text{conv}}$  of a given region, according to equation 9. As discussed in §2.3.1, a value of 1/3 for the total power in compressive turbulence (compression or expansion) is expected in fully isotropic and homogeneous turbulence in equipartition, and thus a value of 1/6 is expected for  $f_{\text{conv}}$ .

## 2.4. Tidal field

When an extended body resides in a gravitational field, different mass elements experience slightly different gravitational forces. In the rest frame of the body, this difference translates to compression or expansion along different directions. The tidal field is in general not isotropic, and can be compressive or expansive in different directions. In principle, it can be fully compressive (i.e. compressive in every direction), but not fully expansive (see below).

Fully compressive tides can arise in systems which reside in cosmological environments (Renaud et al. 2009), but can also arise internally in isolated systems, even in smooth density profiles (Dekel et al. 2003). If a patch of the disk resides in a region where the tidal field is fully compressive, the turbulence in this region can become dominated by compression (Renaud et al. 2014), and this region may undergo a gravitational collapse due to the tides, eventually forming a giant clump. Mathematically, the tidal field is quantified by the tidal tensor, to be explained next.

The first order approximation for the gravitational acceleration about a point  $\mathbf{r}_0$  is

$$F_j(\mathbf{r}_0 + \delta\mathbf{r}) = F_j(\mathbf{r}_0) + \frac{\partial F_j}{\partial r_i} \delta r_i + \dots, \quad (11)$$

where we have employed the summation notation. If  $\phi(\mathbf{r})$  is the gravitational potential, then  $F_j = -\partial\phi/\partial r_j$ , and we can rewrite the acceleration, to first order, as

$$F_j(\mathbf{r}_0 + \delta\mathbf{r}) \approx - \left. \frac{\partial\phi}{\partial r_j} \right|_{\mathbf{r}_0} - \left. \frac{\partial^2\phi}{\partial r_i \partial r_j} \right|_{\mathbf{r}_0} \delta r_i. \quad (12)$$

We define the tidal tensor as  $T_{ij} = \partial^2\phi/\partial r_i \partial r_j$ . Under this definition, the first order approximation for the gravitational acceleration is:

$$F_j(\mathbf{r}_0 + \delta\mathbf{r}) \approx F_j(\mathbf{r}_0) - T_{ij} \delta r_i. \quad (13)$$

The tidal tensor is a symmetric tensor, and therefore there is an orthogonal basis that diagonalizes  $T_{ij}$ . The eigenvalues are real, and we order them by value  $\lambda_1 \geq \lambda_2 \geq \lambda_3$ . Using our definition, a positive eigenvalue represents compression along the direction of its corresponding eigenvector, while a negative value

represents expansion along this direction<sup>9</sup>. If all eigenvalues are positive, the tidal field is said to be fully compressive. Since  $\lambda_1 + \lambda_2 + \lambda_3 = \text{trace}(T) = \nabla^2\phi = 4\pi G\rho \geq 0$ ,  $\lambda_1$  is necessarily positive (i.e. the tidal field cannot be fully expansive), while  $\lambda_2, \lambda_3$  can be either positive or negative.

To quantify the compressiveness of the tidal field, we define a quantity  $f_{\text{tides}}$  as follows. Assume a spherical region of size  $R$  and constant density. As stated above, the tidal tensor is symmetric, and therefore we can align the coordinate system with its three eigenvectors. The mean value of the acceleration along the radial direction (indicative of compression/expansion) is then

$$\begin{aligned} F_t &= -\frac{1}{4\pi/3R^3} \int \left( \overleftrightarrow{T} \mathbf{r} \right) \cdot \frac{\mathbf{r}}{r} d^3\mathbf{r} = -\frac{1}{4\pi/3R^3} \int T_{ij} r_j \frac{r_i}{r} d^3\mathbf{r} \\ &= -\frac{1}{4\pi/3R^3} \int \frac{\lambda_1 x^2 + \lambda_2 y^2 + \lambda_3 z^2}{r} d^3\mathbf{r} = -\frac{1}{4} R (\lambda_1 + \lambda_2 + \lambda_3) \\ &\equiv -\frac{1}{4} R \lambda_1 (1 + f_{\text{tides}}), \end{aligned}$$

where we have defined

$$f_{\text{tides}} = \frac{\lambda_2 + \lambda_3}{\lambda_1}. \quad (14)$$

This simple calculation motivates us to use  $f_{\text{tides}}$  as a quantification of how compressive or expansive the tidal field is in a given spherical region - if  $f_{\text{tides}} > 0$ , then the tidal field is substantially compressive along at least two directions (those of  $\lambda_1$  and  $\lambda_2$ ), and potentially fully compressive. If  $f_{\text{tides}} < 0$ , at least along one direction (that of  $\lambda_3$ ), and potentially two directions (those of  $\lambda_2$  and  $\lambda_3$ ), the tidal field is substantially expansive<sup>10</sup>. As an example, for a spherically symmetric density profile,  $f_{\text{tides}} = 2 - \alpha(r)$ , where  $\alpha(r)$  is the logarithmic slope of the average density within  $r$  (Dekel et al. 2003). For values of  $\alpha = 0, 1, 2, 3$ , corresponding to a flat core, a cuspy profile, an isothermal sphere and a point mass, respectively,  $f_{\text{tides}} = 2, 1, 0, -1$ . Indeed, for a cored profile and a cuspy profile, the average tidal field is compressive. For a cored profile it is fully compressive in all three directions, while for a cuspy profile it is zero along the radial direction and compressive along the other two directions. For an isothermal sphere, the tidal field along the radial direction is expansive and equal in magnitude to the force along the other two directions, which are compressive. The average tidal force is thus zero. Finally, for a point mass, the tidal force along the radial direction is the strongest, and is expansive.

To calculate the compressiveness of the tidal field in a particular region in our simulations, we first dump the gravitational potential onto the same grid uniform grid as in §2.3.2, and calculate the Hessian matrix using a second order, central finite differences method. We then diagonalize the matrix at every grid cell (using the known analytical equations for  $3 \times 3$  matrices) to get the three eigenvalues for each cell. Finally, we perform a volume-weighted average of each eigenvalue inside the given region, and plug the values into the definition of eq. 14, to get  $f_{\text{tides}}$  for each region of interest.

<sup>9</sup> Note that other publications (e.g. Renaud et al. 2009) defined the tidal tensor with a minus sign. Under such definition, a positive (negative) eigenvalue represents disruption (compression) rather than compression (disruption).

<sup>10</sup> Our calculation resulted in  $F_t = -R\lambda_1(1 + f_{\text{tides}})$ , which is positive only when  $f_{\text{tides}} < -1$ , meaning that the mean acceleration is positive only when  $f_{\text{tides}} < -1$ . Nevertheless, substantial tidal stripping can occur along a particular direction even if the mean acceleration is negative.

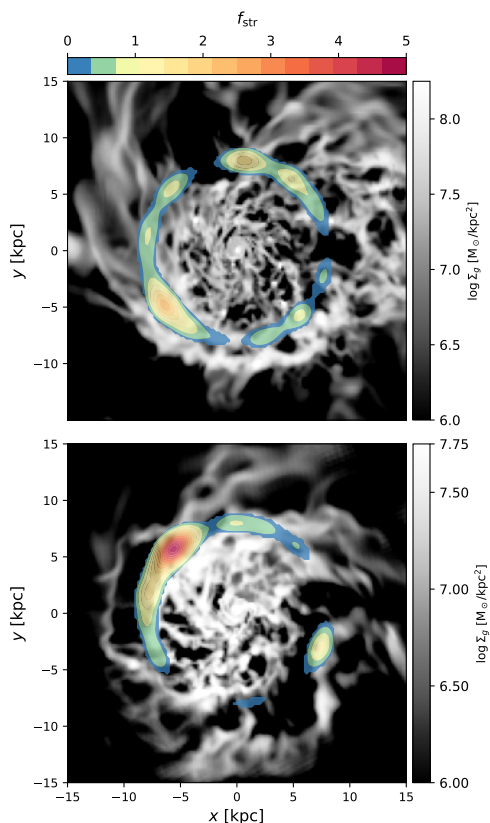


**Fig. 1.** Proof of concept for  $f_{\text{str}}$ . The background color shows the projected surface density of gas in V07 at  $z \sim 2$  (top) and in V08 at  $z \sim 1$  (bottom). The contours are of  $f_{\text{str}}$  in angular bins at a radius of 8 kpc in both panels. We can see how  $f_{\text{str}}$  increases in regions where the stream interacts with the disk.

### 2.5. Stream-disk interaction

When the streams interact with the disk, intense shocks are expected to occur and turbulence is expected to be stirred (Ginzburg et al. 2022), especially if the streams are dense and clumpy due to fragmentation (Klessen & Hennebelle 2010; Forbes et al. 2023). Indeed, an ongoing series of papers, studying the evolution of cold streams feeding massive halos, has revealed that streams are expected to fragment into dense clumps, either gravitationally (Mandelker et al. 2018; Aung et al. 2019), or due to cooling (Mandelker et al. 2020; Aung et al. 2024). Furthermore, since the streams flow towards the central galaxy in the potential of the dark matter halo, gravitational focusing tends to make the streams narrower and denser as they reach the disk (Aung et al. 2024). Thus, we expect regions of the disk that interact with streams to be sites of high compressive turbulence that can lead to clump formation. This was briefly discussed in M24, and can be seen in figure 3 therein. The degree to which stream-disk interaction drives turbulence is a subject of an ongoing work (Ginzburg et al. 2022, Ginzburg et al., in prep).

In the current work, we want to understand whether or not protoclump regions are also sites of stream-disk interaction, and how the local fraction of compressive turbulence in these regions differs from other regions in the disk that do not interact with streams. The VELA simulations are AMR hydro simulations that do not have tracer particles. It is therefore difficult to determine whether a mass element was recently brought by accretion or has been part of the disk for a long time. We therefore use the

approximate streamline method developed by Dutta Chowdhury et al. (2024). In short, by assuming that the gas velocity field is roughly constant over a disk dynamical time, gas cells in a given snapshot can be traced using the gas velocity data of that snapshot only. Starting from its current 3D position, a gas cell in a given snapshot is traced back in time along its streamline to yield an approximate initial 3D position one dynamical time ago. If the distance between the initial and current positions is larger than 10% the disk radius, we tag this cell as a stream material. We refer the reader to Dutta Chowdhury et al. (2024) for a more elaborate description of the method.

To quantify whether or not a given protoclump region resides in a site where a stream is interacting with the disk, we look at an annulus at the same radius of the protoclump, with its width being the size of the protoclump, namely  $\Delta R = 2R_{\text{PC}} = 1$  kpc. We then divide the annulus to angular bins of angular opening  $\Delta\theta = d_{\text{PC}}/r_{\text{PC}}$ , where  $d_{\text{PC}} = 1$  kpc is the diameter of the protoclump region, and  $r_{\text{PC}}$  is the distance of the protoclump region from the galactic center. We then define

$$f_{\text{str}} = \frac{M_{\text{stream,PC}}}{\langle M_{\text{stream,slice}} \rangle}, \quad (15)$$

where  $M_{\text{stream,PC}}$  is the total mass of stream material in the protoclump's angular bin, and  $\langle M_{\text{stream,slice}} \rangle$  is the average stream mass in all angular bins within the annulus. In figure 1 we show contours of  $f_{\text{str}}$  at 8 kpc from V07 at  $z \sim 2$  and from V08 at  $z \sim 1$ . We can see the stream from the top left joining the disk, resulting in an increased  $f_{\text{str}}$  where the stream joins the disk.

## 3. Results

We want to test whether or not protoclump regions form in regions with fully compressive tides and/or in sites of stream-disk interaction. Furthermore, we would like to quantify the fraction of energy in compressive modes in such regions, and in converging modes in particular, and compare to the excess in converging modes found in protoclump regions in M24. In order to differentiate protoclumps from the underlying disk, we associate to each protoclump a random patch that has the same distance from the galactic center and of the same size as the protoclump region, making sure it does not overlap with other protoclump regions. In the following analysis, we analyze protoclumps corresponding to clumps with a maximal baryonic mass larger than  $10^8 M_{\odot}$ , similar to M24. We calculate  $f_{\text{conv}}$ ,  $f_{\text{ides}}$  and  $f_{\text{str}}$  as defined in eqs. 9, 14 and 15 for the protoclump regions and the random patches in the disk, as outlined at the end of §2.3.2, §2.4 and §2.5.

In §3.1 we analyze the global fraction in compressive modes as a function of time. In §3.2 we compare the various quantities between protoclumps and their corresponding random patches, and in §3.3 we correlate the different quantities against the  $f_{\text{conv}}$ .

### 3.1. Global fraction of compressive turbulence

In figure 2, we show the fraction of turbulent energy in converging or compressive (converging plus diverging) modes, averaged over the whole disk, as defined in eq. 10, as a function of the cosmological scale factor. We show the evolution of three out of the eight galaxies we analyze. We can see that, most of the time, the total fraction of energy in the compressive mode is about 1/3 (blue curve), as expected in fully isotropic and homogeneous turbulence in equipartition (see §2.3.1). The red curve shows only



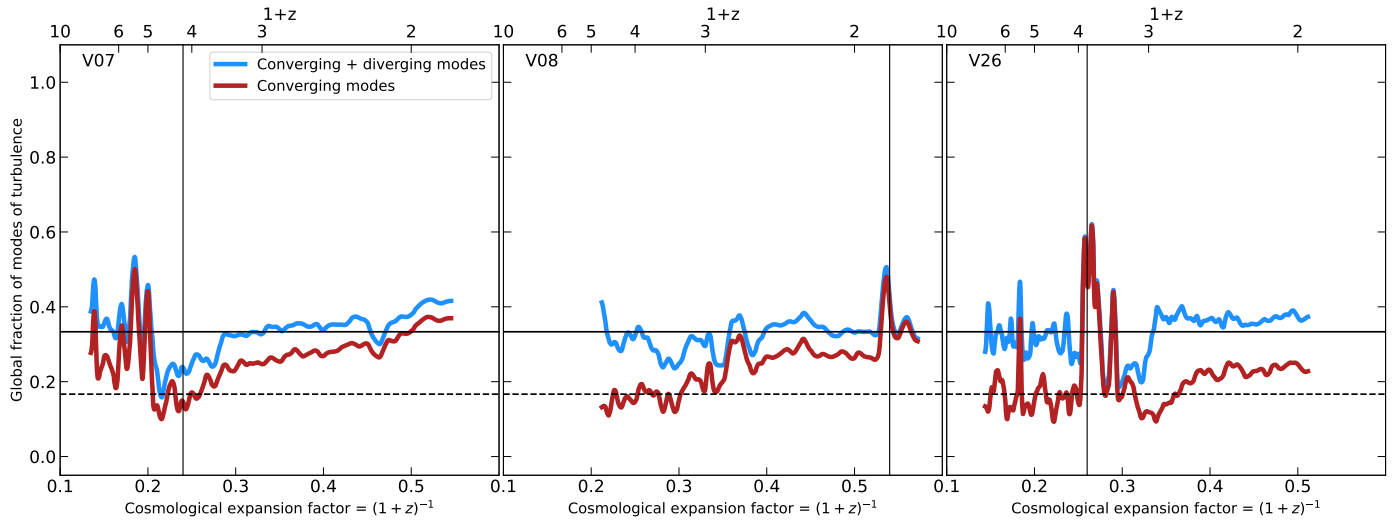


**Fig. 2.** The temporal evolution of the global fraction of turbulent energy in converging and diverging (blue curve) and only converging (i.e. only cells with  $\nabla \cdot \mathbf{v} < 0$ ; red curve) flows, for three galaxies from our suite. The vertical black line indicates the moment of the blue nugget phase in each galaxy (Lapiner et al. 2023). The horizontal solid (dashed) lines indicate one third (sixth) of the total energy, values expected for fully isotropic and homogeneous turbulence in equipartition. Each of the blue nugget phases are preceded by at least one major merger, which increases the global fraction in compressive turbulence, before settling back to the equilibrium values.

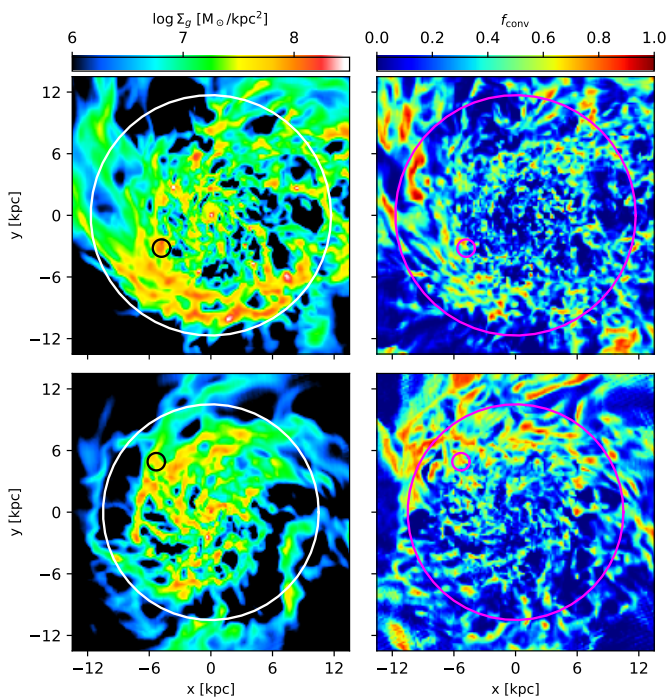


**Fig. 3.** Correlation of  $f_{\text{conv}}$  with gas density in protoclump regions. In the left panels, we show the projected surface density of the gas. The top row represents V07 at  $z \sim 2$  while the bottom row represents V08 at  $z \sim 1$ , as in figure 1. The black circles indicate the location of a protoclump region. The white circle is the disk radius, defined as the radius that contains 85% of the cold gas in the disk. In the right panels, we show maps of  $f_{\text{conv}}$  in the same snapshot. The small magenta circle shows the location of the same protoclump region, while the large magenta circle is the disk radius. We can see that inside the region of the protoclump, most of the mass has  $f_{\text{conv}} \sim 0.5 - 0.8$ . Furthermore, we see that the protoclump regions are close to where the stream joins the disk (see §2.5 and figure 1).

the fraction in converging modes, i.e. only for cells with negative divergence. We can see that for V26 it is close to 1/6, while for V07 it is usually around 0.3. For V08, at early times, the total fraction of energy in converging modes is around 1/6, increasing to 1/3 at later times.

Each of these galaxies undergoes a compaction event that leads to a blue nugget (Zolotov et al. 2015), which is usually preceded by a major merger (Lapiner et al. 2023). We can see that before the major mergers and the subsequent compaction events occur, the fraction of energy in compressive modes (converging plus diverging) is roughly 1/3, as expected in a fully isotropic and homogeneous turbulence in equipartition<sup>11</sup>. During the merger, we can see a sharp increase in the fraction of energy in global compression, similar behavior as seen in idealized simulations of galactic mergers (Renaud et al. 2014).

Overall, we strengthen the result of M24 that globally, the turbulence field does not deviate much from the equilibrium ratios, except when undergoing major mergers and compaction events.

### 3.2. Protoclumps vs. random patches

We now turn to the local analysis in small regions in the disk. We start by comparing  $f_{\text{conv}}$ ,  $f_{\text{tides}}$  and  $f_{\text{str}}$  between protoclump regions and random patches (as explained in the beginning of this section).

#### 3.2.1. Compressive turbulence

In figure 3 we show examples of snapshots from V07 and V08 at redshifts  $z \sim 2$  and 1, respectively. The small black (magenta) circle in the left (right) panel marks a protoclump region. We can see that the protoclump regions reside in a part of the disk that

<sup>11</sup> As can be seen in figure 1 in Renaud et al. (2014), a galaxy in isolation attains equipartition within a couple of dynamical times.

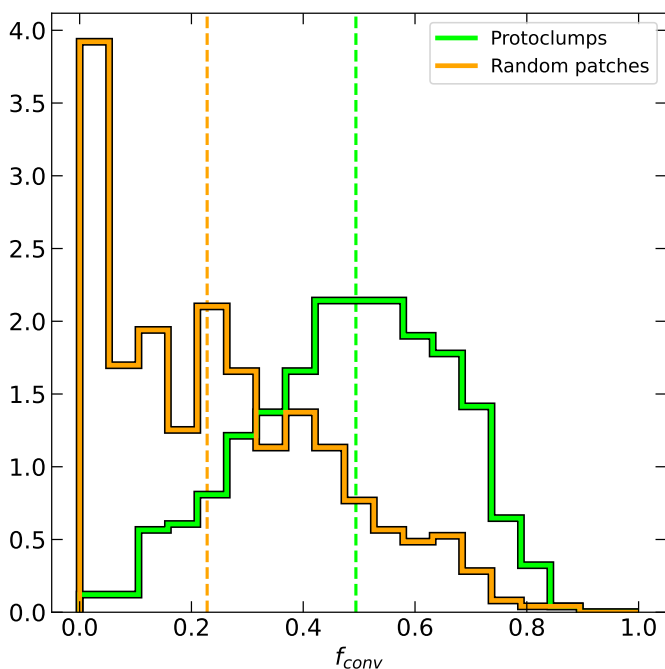


**Fig. 4.** The probability distribution of  $f_{\text{conv}}$  in protoclump regions (green histogram) and random patches (orange histogram) over all eight galaxies. The vertical lines of each color indicate the median of the corresponding distribution. We can see that protoclump regions have a median  $f_{\text{conv}} \sim 0.5$ , while random patches have a median  $f_{\text{conv}} \sim 0.21$ , meaning that protoclump regions have a strong excess in converging modes, compared to random patches in the disk, which are more inline with equilibrium values.

interacts with a stream that comes from the top left corner (see also figure 1). As we have argued above, this interaction stirs up turbulence, induces compression by local shocks and boosts the fraction of energy in converging modes, as clearly seen in the right panel of figure 3, which shows the mass weighted projection of  $f_{\text{conv}}$ .

In figure 4, we show the distribution of  $f_{\text{conv}}$  in all protoclump regions and their corresponding random patches, for all of the eight galaxies. We can clearly see that  $f_{\text{conv}}$  has very different distributions in protoclumps and random patches - protoclump regions have a median  $f_{\text{conv}} \sim 0.5$ , larger than the expected equilibrium value, while random patches have a median of  $f_{\text{conv}} \sim 0.21$ , which is more in line with the expected equilibrium value of  $\sim 0.16$ . These results strengthen our results from M24, in which the analysis was performed only on V07.

### 3.2.2. Tides

In the left panel of figure 5, we show the distribution of  $f_{\text{tides}}$  in protoclump regions and random patches. Recall from §2.4 that a positive value of  $f_{\text{tides}}$  is indicative of a substantial or fully compressive tidal field, while a negative value hints at substantial stripping along some direction. Figure 5 clearly shows that  $f_{\text{tides}}$  has different distributions among protoclumps and random patches. While random patches have a median  $f_{\text{tides}} \sim -0.26$ , protoclump regions have a median  $f_{\text{tides}} \sim 0.32$ , with the vast majority of protoclumps having  $f_{\text{tides}} > 0$ .

In the right panel of figure 5, we show the distribution of  $\lambda_3$  (arbitrarily scaled, see caption) in protoclump regions and ran-

dom patches. Although the distribution is of  $\log \lambda_3$ , negative values on the x-axis represent negative values of  $\lambda_3$  rather than values  $0 < \lambda_3 < 1$  (see caption). We can see that the tidal field in  $\sim 25\%$  of the protoclumps is fully compressive, since  $\lambda_3 > 0$  and therefore all of the eigenvalues of the tidal tensor are positive. On the other hand all of the random patches have  $\lambda_3 < 0$ , meaning that the tidal field is expansive along at least one direction.

We conclude from figure 5 that almost all of the protoclumps reside in regions where the tidal field is substantially compressive, and almost exclusively, regions with fully compressive tides are protoclumps.

### 3.2.3. Stream-disk interaction

In figure 6, we show the distribution of  $f_{\text{str}}$  in protoclump regions and in their corresponding random patches. Random patches have, on average,  $f_{\text{str}} \sim 0.8$ , meaning that the stream mass in their vicinity is slightly less than the average over the annulus. For protoclump regions, we find on average  $f_{\text{str}} \sim 2.5$ , with a broad tail reaching  $f_{\text{str}} \sim 10$ , i.e. some protoclump regions have ten times more stream material than the average at their galactocentric radius, indicating that they reside in a site of stream-disk interaction.

The distributions of  $f_{\text{str}}$  in protoclumps and random patches are more similar than they are for both  $f_{\text{conv}}$  and  $f_{\text{tides}}$ , as can be seen by comparing figures 4 and 5 (left panel) to figure 6. However, a major caveat to our definition of  $f_{\text{str}}$  is the noisy definition of stream material compared to disk material, due to the lack of tracer particles in our simulations (Dutta Chowdhury et al. 2024). Furthermore, an energy-based or momentum-based quantity would perhaps be more appropriate than the mass-based quantity we use here, however without tracer particles these will suffer similar uncertainties. Nevertheless, we find that  $f_{\text{str}} = 1$  is around the 30-th percentile of the distribution for protoclump regions, meaning that around 70% of the protoclumps reside in sites of stream-disk interaction, compared to only  $\sim 40\%$  of random patches.

### 3.3. $f_{\text{tides}}$ and $f_{\text{str}}$ vs. $f_{\text{conv}}$

In the previous section, we have found that protoclump regions tend to reside in regions where the turbulent velocity field is locally compressive (§3.2.1), tides are substantially or fully compressive (§3.2.2), and are sites of stream-disk interaction (§3.2.3). We now attempt to answer the question whether the tides or the stream-disk interactions cause the excess compression in the turbulent velocity field. In our current numerical setting it is not straightforward to draw causal conclusions on whether the tides or the stream-disk interaction are responsible for the excess of compressive turbulence. We therefore look at correlations between the quantities, leaving a more detailed physical analysis to future work (Ginzburg et al., in prep).

The left panel of figure 7 shows  $f_{\text{tides}}$  vs.  $f_{\text{conv}}$  for protoclumps and random patches. We can see that the median values of  $f_{\text{tides}}$  in bins of  $f_{\text{conv}}$  increase with increasing  $f_{\text{conv}}$ , from  $f_{\text{tides}} \lesssim 0$  at  $f_{\text{conv}} \sim 0.1$  to  $f_{\text{tides}} \sim 0.5$  at  $f_{\text{conv}} \sim 0.65$ . The Spearman correlation coefficient between  $f_{\text{tides}}$  and  $f_{\text{conv}}$  is found to be  $\sim 0.46$ . It is also evident from the left panel of figure 7 that protoclumps mostly occupy the upper right quadrant, that of high  $f_{\text{conv}}$  and positive  $f_{\text{tides}}$ , while random patches mostly occupy the bottom left quadrant, that of low  $f_{\text{conv}}$  and negative  $f_{\text{tides}}$ .



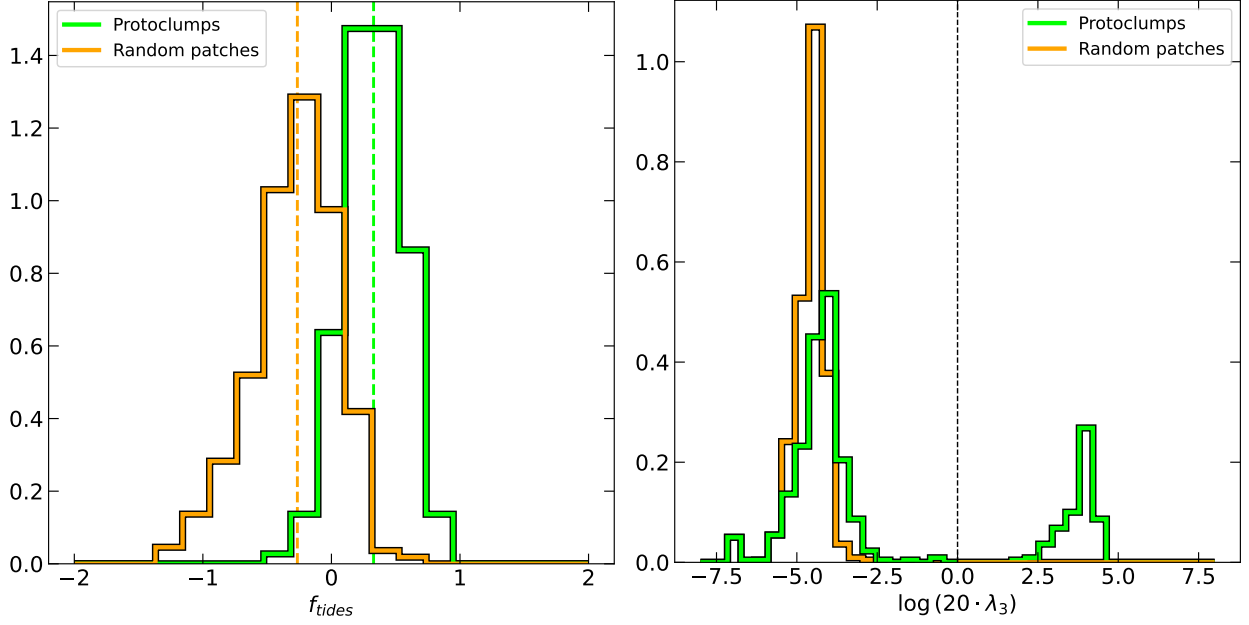


**Fig. 5.** Probability distributions of  $f_{\text{tides}}$  (left) and  $\lambda_3$  (right) in protoclump regions (green histograms) and random patches (orange histograms). *Left:* The vertical lines of each color indicate the median of the corresponding distribution, 0.33 and  $-0.27$  for protoclumps and random patches, respectively.  $f_{\text{tides}}$  in protoclump regions is mostly positive, indicating substantial or fully compressive tides, while random patches mostly have  $f_{\text{tides}} < 0$ , indicating substantial stripping. *Right:*  $\lambda_3$  was scaled by 20 in order to separate negative and positive values and present them in a logarithmic scale. Negative values are actually  $-\log(-20 \cdot \lambda_3)$  (e.g. a value of  $-5$  along the x-axis represents  $-10^5$ ).  $\lambda_3$  is positive almost exclusively in protoclump regions, and about  $\sim 25\%$  of the protoclump regions have  $\lambda_3 > 0$ , implying fully compressive tides.

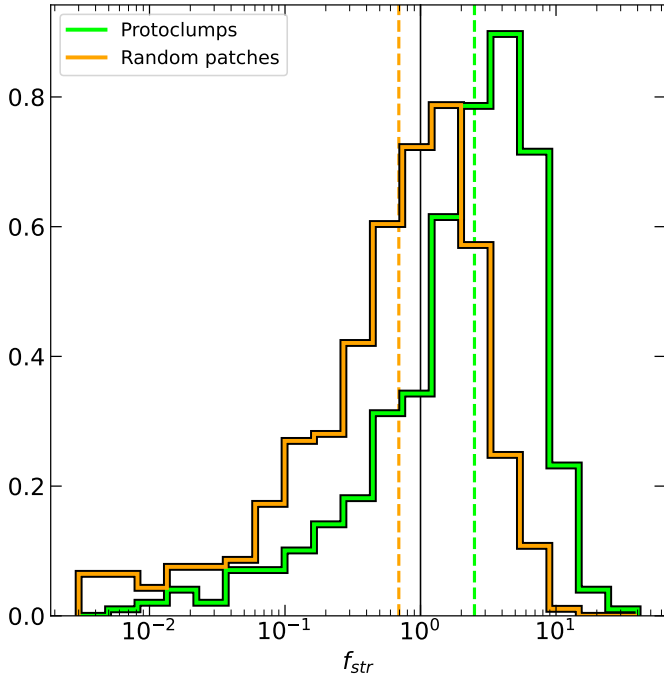


**Fig. 6.** Same as figure 4, but for  $f_{\text{str}}$ , which measures the amount of stream mass in a given region (see text). The vertical black line is at  $f_{\text{str}} = 1$ . We can see that protoclump regions tend to have larger  $f_{\text{str}}$  than random patches, indicating that they reside in regions with intense accretion. The median  $f_{\text{str}}$  for protoclumps is 2.5, while for random patches it is 0.8.

The right panel of figure 7 shows  $f_{\text{str}}$  vs.  $f_{\text{conv}}$  for protoclumps and random patches. Again, we can see a positive cor-

relation between these two quantities.  $f_{\text{str}} \sim 1$  at  $f_{\text{conv}} \sim 0.1$  and increases to  $f_{\text{str}} \sim 2$  at  $f_{\text{conv}} \sim 0.65$ . It is evident that the scatter in  $f_{\text{str}}$  is very large, which we attribute to the noisy definition we employ for stream material. The Spearman correlation coefficient between  $f_{\text{str}}$  and  $f_{\text{conv}}$  is found to be 0.3. Here also protoclump regions mostly occupy the high  $f_{\text{conv}}$  high  $f_{\text{str}}$  quadrant, while random patches mostly occupy the low  $f_{\text{conv}}$  low  $f_{\text{str}}$  quadrant.

## 4. Discussion

### 4.1. Source of gravitational tides - cosmological vs. isolated simulations

In figure 5, we showed that almost all of the protoclumps reside in regions where the tidal field is substantially or fully compressive, and almost all of the regions where the tidal field is fully compressive are protoclumps regions. Furthermore, in the left panel of figure 7, we showed a positive correlation between the compressive tendency of the tidal field and the compressive tendency of the local turbulent field. A key motivation for examining the tidal field's impact on compressive turbulence in protoclumps is the distinct difference observed in M24 between isolated and cosmological simulations, and the previous result that the cosmological environment can cause compressive tides that drive compressive turbulence (Renaud et al. 2014). It is therefore important to try and shed some light on the source of the tides in our simulations.

With the findings of several studies (Renaud et al. 2009; Li et al. 2022) that, during major mergers, more regions of the disk experience tidal compression, mergers are a natural candidate for the source of tides. While galaxies in the VELA simulations experience some mergers during their lifetime, they usually experi-

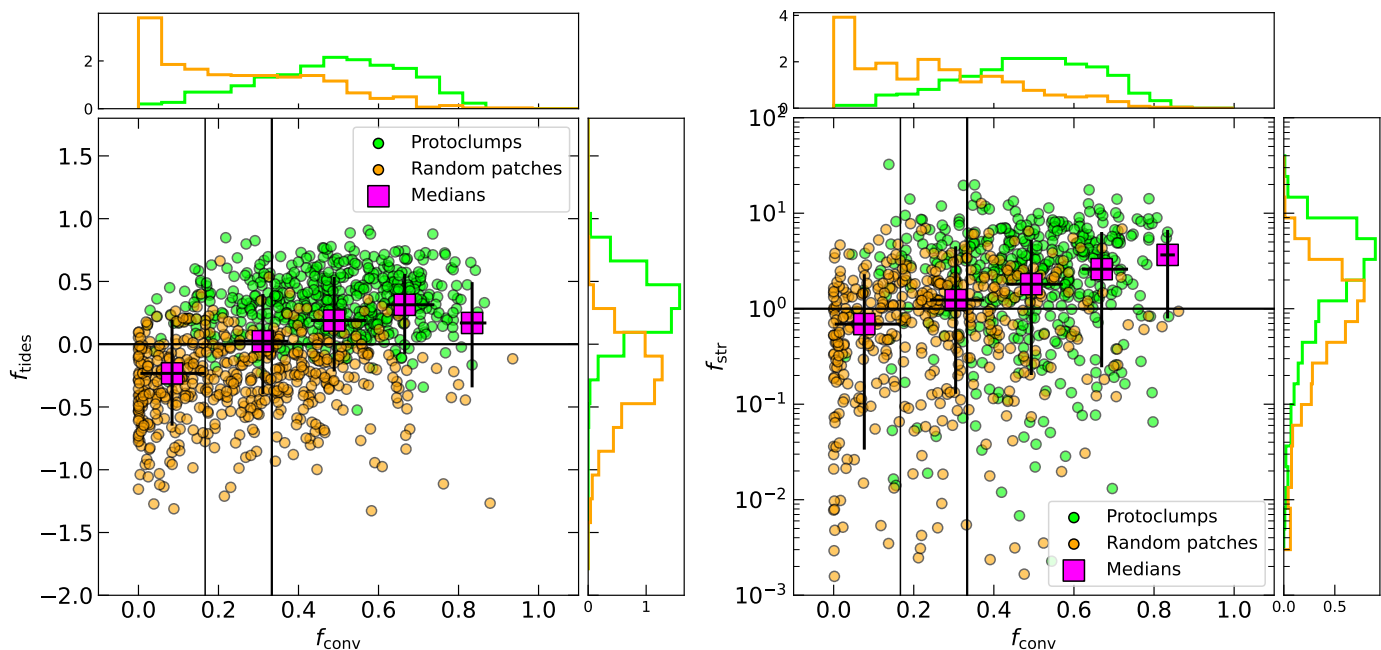


**Fig. 7.** Correlations between  $f_{\text{conv}}$  (x-axis) and  $f_{\text{tides}}$  (left) or  $f_{\text{str}}$  (right). Each point is either a protoclump (green points) or a random patch (orange points). The histograms are the projected distributions of the corresponding quantity. The vertical black lines correspond to  $f_{\text{conv}} = 16\%$  and  $f_{\text{conv}} = 33\%$ . The magenta squares are the medians of all of the points in bins of  $f_{\text{conv}}$ , and the error bars are the 16-th and 84-th percentiles of each quantity. Both  $f_{\text{tides}}$  and  $f_{\text{str}}$  show a positive correlation with  $f_{\text{conv}}$ . The Spearman correlation coefficient for  $f_{\text{tides}}$  and  $f_{\text{str}}$  against  $f_{\text{conv}}$  are 0.46 and 0.3 respectively. Furthermore, protoclump regions occupy the upper-right quadrants in both panels.

ence around one major merger (Dekel et al. 2020; Lapiner et al. 2023), not sufficient to explain our results here. Moreover, this would have led to a systematic increase in the global power in compressive modes (Renaud et al. 2014), which is not observed. However, compressive tides can arise due to other sources as well. For example, from the potential of the galaxy or its host halo - in a cored spherical density profile (i.e. with a negative logarithmic slope less than unity), the tidal force in becomes fully compressive (Dekel et al. 2003). In a flattened, axisymmetric system, the tidal force in the radial direction in the mid-plane becomes compressive if the gravitational potential satisfies  $\partial^2\phi/\partial R^2 > 0$ . In general, the tidal field will be compressive along any direction in which the gravitational field increases with increasing distance from the region of interest. Given the small number of major mergers in our simulations, the potential of the dark halo or the smooth component of the disk, nearby perturbations in the disk, such as clumps, spiral arms or other overdensities, minor mergers or the generally messy environment in which the galaxy resides are more likely sources for compressive tides.

To test the viability of in-situ induced compressive tides, we perform our tidal analysis on the same isolated simulations we analyzed in M24. This simulation is an idealized simulation of a star forming galactic disk with baryonic mass of  $\sim 3.2 \cdot 10^{10} M_{\odot}$  and initial 65% gas fraction. We refer the reader to §2.2 of M24 for details on the simulation. In figure 8, we show the analog of figure 5, but for the isolated simulation. We see that the distributions of both  $f_{\text{tides}}$  and  $\lambda_3$  are qualitatively different in the isolated simulation compared to VELA. First, in the isolated simulation the distribution of  $f_{\text{tides}}$  is very similar in protoclumps and random patches, with a median value of  $\sim 0.2$ . Second, all protoclumps in the isolated simulation reside in regions where  $\lambda_3 < 0$ , that is, no protoclump experiences fully compressive tides.

While this is not conclusive evidence, the comparison suggests that the compressive tides in the VELA simulations likely do not originate from the potential of the halo or of the smooth disk component. However, since the clump-forming phase of the disk in the isolated simulation is relatively short, whereas in the VELA simulations it is a continuous process, we cannot rule out internal perturbations, as noted above, as potential sources of the tides. A more detailed analysis is required to identify whether the tides arise from internal or external perturbations, which is beyond the scope of this paper.

#### 4.2. Efficiency of stream-driven turbulence

When streams interact with a galactic disk, we expect them to drive turbulence within the disk. However, the efficiency of this stream-driven turbulence remains a topic of debate. Some studies suggest that accretion has little to no effect on disk turbulence (Hopkins et al. 2013), while others argue that its impact is weak (Elmegreen & Burkert 2010), occasionally significant (Gabor & Bournaud 2014), or even highly efficient (Forbes et al. 2023; Jiménez et al. 2023). If accretion-driven turbulence is indeed efficient, it could play a major role in sustaining overall disk turbulence (Ginzburg et al. 2022), particularly compressive turbulence. Preliminary controlled experiments investigating streams feeding a galactic disk (Ginzburg et al., in prep) indicate that disks fed by streams tend to sustain larger values of velocity dispersions, with a strong dependence on the density of the incoming streams.

Stream density is expected to play a key role (Klessen & Hennebelle 2010), as basic momentum conservation suggests that more kinetic energy is retained in the system when the den-

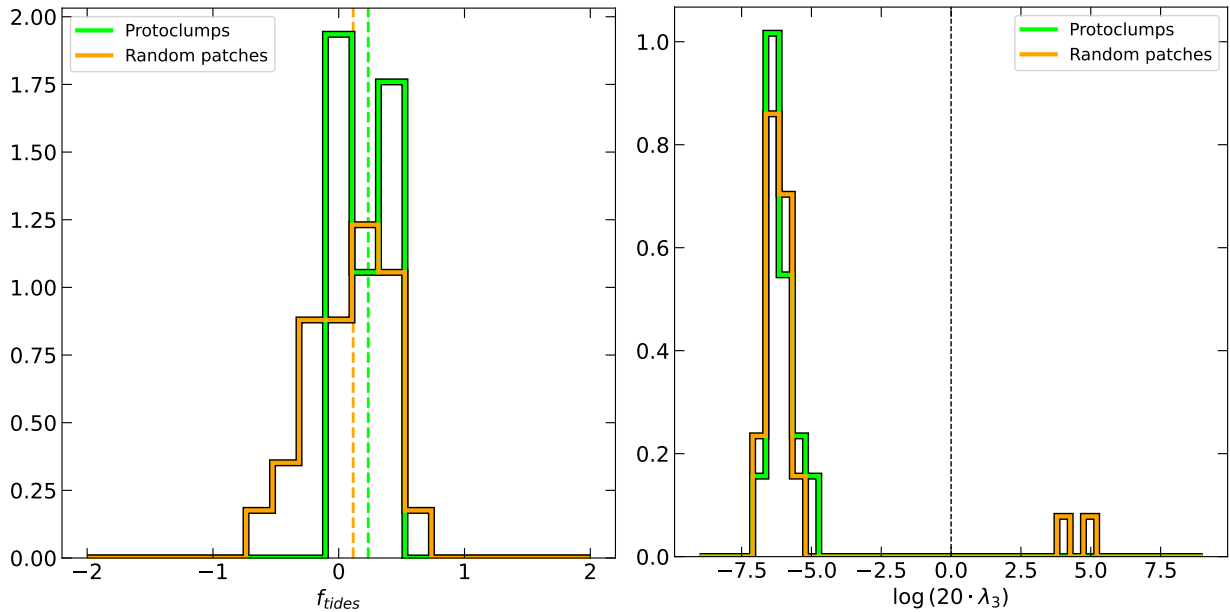


**Fig. 8.** The same as figure 5, but for the protoclumps in the isolated galaxy simulation. We can see that the protoclumps in the isolated galaxy simulation are in regions where the tidal field is only weakly compressive, and are not much different than the random patches. Furthermore,  $\lambda_3 < 0$  for all of the protoclump regions, as opposed to protoclump regions in the cosmological simulations.

sities of the colliding materials are comparable<sup>12</sup>. Since the disk is built by the incoming material, streams cannot be much less dense than the outer disk. Moreover, simulations of streams feeding massive halos show that streams grow denser as they approach the inner halo (Aung et al. 2024), undergoing gravitational fragmentation along the way (Mandelker et al. 2018; Aung et al. 2019). Furthermore, Folini et al. (2014) found in simulations of head on collision of isothermal flows that high Mach number collisions are efficient at converting collision kinetic energy to turbulent kinetic energy, and produce a broader density distribution in the collision region.

Future work is planned to explore stream-disk interactions and the efficiency of accretion-driven turbulence, from cloud to galactic scales. These studies will also shed light on how compressive turbulence is driven in sites of stream-disk interaction.

#### 4.3. Definition of compressive modes of turbulence

The motivation for the definition of  $f_{\text{conv}}$  as defined in eq. 9, is based on the Taylor expansion performed in eq. 5 (see also Appendix B). This definition neglects the shearing term, which we termed  $\overleftrightarrow{S}$ , which is perhaps justified only for periodic or vanishing boundary conditions (Kritsuk et al. 2007), both of which are clearly irrelevant for our local analysis. We can gain qualitative insights on the relevance of  $\overleftrightarrow{S}$  from the following argument.

The matrix  $\overleftrightarrow{S}$  is a symmetric matrix, and hence can be orthogonally diagonalized by three real eigenvalues,  $\mu_1 \geq \mu_2 \geq \mu_3$ . Furthermore, it is traceless, meaning that  $\mu_1 + \mu_2 + \mu_3 = 0$ . It therefore follows that  $\mu_1 \geq 0 \geq \mu_3$ , with  $\mu_2$  somewhere in be-

tween. It means that the contribution from  $\overleftrightarrow{S}$  along the direction corresponding to  $\mu_3$  is converging, while the contribution from  $\overleftrightarrow{S}$  along the direction corresponding to  $\mu_1$  is diverging. Since the sum of the eigenvalues is zero,  $\mu_1$  and  $|\mu_3|$  can only differ at most by a factor of two. Thus, assuming  $\mu_1 \sim |\mu_3|$  is a reasonable approximation. We can then write the Taylor expansion of eq. 5 in the coordinate system determined by  $\overleftrightarrow{S}$  as

$$\mathbf{v}(\mathbf{r} + \delta\mathbf{r}') \approx \mathbf{v} + \begin{pmatrix} (1/3 (\nabla \cdot \mathbf{v}) + \mu_1) \delta x' \\ 1/3 (\nabla \cdot \mathbf{v}) \delta y' \\ (1/3 (\nabla \cdot \mathbf{v}) - \mu_1) \delta z' \end{pmatrix} + \frac{1}{2} \boldsymbol{\omega}' \times \delta\mathbf{r}', \quad (16)$$

where primed values are the vectors in the lab frame represented in the coordinate frame of  $\overleftrightarrow{S}$ . It is therefore evident that neglecting  $\overleftrightarrow{S}$  is reasonable only if  $|\nabla \cdot \mathbf{v}| \gg \mu_1$ . However, for a region to become dense enough for self gravity to become efficient, isotropic collapse is not needed. It is therefore enough that  $\nabla \cdot \mathbf{v} < 0$  and  $|\nabla \cdot \mathbf{v}| \gtrsim \mu_1$  so that the flow along the  $x'$  will be weakly diverging, and converging flow will occur along  $y'$  and  $z'$  direction.

When examining the simulations, we find that indeed usually  $\mu_2 \sim 0$ , while  $\mu_1 \sim |\mu_3|$ . protoclump regions usually have smaller shear eigenvalues than other random patches in the disk. Furthermore, we find that  $|\nabla \cdot \mathbf{v}| \sim 2\mu_1$  in protoclumps, while  $|\nabla \cdot \mathbf{v}| \lesssim \mu_1$  in random patches. Alongside the sub-dominance of converging modes in random patches, we conclude that shear has a weaker effect in protoclump regions compared to random patches, which are more susceptible to shear, which prevents clump formation even when stellar feedback is weak (Fensch & Bournaud 2020).

A more robust, multi scale method is required to go beyond the Helmholtz decomposition and Taylor approximation. A natural candidate is by utilizing wavelet transforms, which are common in turbulence studies in fluid dynamics (Farge 1992), but seem to be less common in galactic fluid dynamics. Not only that, but a locally orthogonal Helmholtz-like decomposition algorithm using wavelets has been formalized (Deriaz & Perrier

<sup>12</sup> For instance, in a simple, perfectly inelastic collision, the fraction of kinetic energy retained in the system is proportional to  $\delta/(1 + \delta)$ , where  $\delta$  is the density contrast between the colliding materials. While this relationship may differ in fluid collisions, it highlights the significance of density contrast in such interactions.



2009). Future work will be dedicated to performing turbulence decomposition using wavelets, with the potential for a more self-consistent quantification of compressive and solenoidal modes of turbulence.

## 5. Conclusions

By analyzing cosmological simulations of violent disks at  $1 \lesssim z \lesssim 4$ , we studied the turbulent nature of protoclumps - regions out of which giant, star forming clumps form. Protoclump regions in the VELA cosmological simulations show local values of the Toomre- $Q$  parameter greater than unity, sometimes substantially greater (Inoue et al. 2016), indicating that their subsequent gravitational collapse is not initiated by linear gravitational instabilities. An excess in compressive modes of turbulence, and in particular converging modes, can on the one hand increase the value of the velocity dispersion, and therefore increase  $Q$ , but on the other hand cause the local material to become dense enough for self-gravity to eventually kick in (Hopkins & Christiansen 2013).

By extending the sample size of galaxies and protoclump regions, we strengthened the conclusion of M24, finding that protoclumps are dominated by converging modes of turbulence. In our extended sample, we find that  $\sim 50 - 70\%$  of the turbulent kinetic energy in protoclumps is in converging modes, compared to  $\sim 16\%$  expected in a fully isotropic and homogeneous turbulence in equipartition. Such an excess was not found in isolated galaxies, as we have shown in M24, implying that the cosmological environment or its influence on the galaxy causes its turbulence to be overly compressive.

We examine two external mechanisms for generating the excess of compressive turbulence, namely compressive tides and interactions between the disk and dense streams accreting from the cosmic web. First, the messy environment of galaxies in a cosmological setting, including merging galaxies, gives rise to gravitational tides that can be substantially compressive, and at times fully compressive (Dekel et al. 2003; Renaud et al. 2009; Li et al. 2022). We quantify the compressiveness of the tidal field by the dimensionless quantity  $f_{\text{tides}}$  (eq. 14). We find that almost all protoclump regions have  $f_{\text{tides}} > 0$ , indicating that they reside in regions where the tidal field is substantially compressive, with  $f_{\text{tides}} \sim 0.32$  on average. On the other hand, random patches in the disk have  $f_{\text{tides}} \lesssim 0$ , indicating that the tidal field in these regions is substantially expansive, at least along one direction. Furthermore, we found that  $\sim 25\%$  of the protoclumps reside in regions where the tidal field is fully compressive, while practically no random patches are regions of fully compressive tides.

Second, high redshift massive galaxies in cosmological environments are fed by gaseous streams, typically three (Danovich et al. 2012; Codis et al. 2018). Upon impact, the streams can cause a strong compression due to shocks. We find that around 70% of the protoclump regions are sites of stream-disk interaction, containing  $\sim 2 - 10$  times as much stream material as the average at their galactocentric distance. Random patches, on the other hand, are more typical, with the mass in stream material in them close to the average at their galactocentric distance. We therefore conclude that protoclump regions are distinct, both in terms of experiencing substantially compressive tides and residing in sites of stream-disk interaction.

We then turn to examine how these two mechanisms correlate with the fraction of energy in compressive motion in the protoclumps and random patches in the disk. We find a positive

correlation between the fraction of energy that is in compressive motion to the compressiveness of the tidal field in the region. Regions of the disk in which the tidal field is expansive typically have  $f_{\text{conv}} \sim 0.16$ , which is the value expected for a fully isotropic and homogeneous turbulence in equipartition. As the tidal field becomes more compressive, the fraction of energy in converging modes increases to  $f_{\text{conv}} \sim 0.6 - 0.7$ , on average. Similarly, we find a positive correlation between the intensity of the accreting streams in a given region to the fraction of energy in converging modes in the same region. Regions that are not intensely fed by streams have  $f_{\text{conv}} \sim 0.16$ , while sites of stream-disk interaction have  $f_{\text{conv}} \sim 0.5 - 0.7$ .

Our results suggest that both compressive tides and stream-disk interactions can drive compressive modes of turbulence. A more detailed investigation into the sources of compressive tides is required (see §4.1). However, an initial comparison with an isolated simulation suggests that these tides are not caused by the potential of the dark matter halo or the smooth disk component but instead arise either from external perturbations or from internal perturbations absent during clump formation in the isolated simulations. Furthermore, the lack of tracer particles in the VELA simulations makes the stream identification crude and noisy. We plan to perform a detailed analysis of using cosmological simulations with tracer particles, in order to properly isolate accreted material from the overall gas in the disk.

The results of Inoue et al. (2016), M24 and the current study, suggest that there is a need for a complementary physical theory for clump formation in cosmological disk galaxies. It is evident from these works that Toomre instability does not fully describe disk fragmentation in cosmological contexts. Furthermore, the results of Dutta Chowdhury et al. (2024) indicate that Toomre-based models for radial mass transport (Dekel et al. 2009; Krumholz & Burkert 2010) generally over-predict the radial velocities observed in numerical simulations. While Hopkins & Christiansen (2013) provide a turbulence-dependent stability threshold for  $Q$  based on a statistical analysis, a more thorough analysis, based on first principles, is required.

*Acknowledgements.* This work was partly supported by ISF grant 861/20, BSF-NSF grant 2023723, and by BSF-NSF grant 2023730 and by grant JWST-AR-03305.005-A. The VELA simulations were performed at the National Energy Research Scientific Computing Center (NERSC) at Lawrence Berkeley National Laboratory, and at NASA Advanced Supercomputing (NAS) at NASA Ames Research Center.

## References

- Aung H., Mandelker N., Nagai D., Dekel A., Birnboim Y., 2019, *MNRAS*, **490**, 181
- Aung H., Mandelker N., Dekel A., Nagai D., Semenov V., van den Bosch F. C., 2024, *MNRAS*, **532**, 2965
- Binney J., Tremaine S., 2008, *Galactic Dynamics: Second Edition*
- Bournaud F., Elmegreen B. G., 2009, *ApJ*, **694**, L158
- Brunt C. M., Federrath C., 2014, *MNRAS*, **442**, 1451
- Cava A., Schaerer D., Richard J., Pérez-González P. G., Dessauges-Zavadsky M., Mayer L., Tamburello V., 2018, *Nature Astronomy*, **2**, 76
- Ceverino D., Klypin A., 2009, *ApJ*, **695**, 292
- Ceverino D., Dekel A., Bournaud F., 2010, *MNRAS*, **404**, 2151
- Ceverino D., Dekel A., Mandelker N., Bournaud F., Burkert A., Genzel R., Primack J., 2012, *MNRAS*, **420**, 3490
- Ceverino D., Klypin A., Klimek E. S., Trujillo-Gomez S., Churchill C. W., Primack J., Dekel A., 2014, *MNRAS*, **442**, 1545
- Ceverino D., Mandelker N., Snyder G. F., Lapiner S., Dekel A., Primack J., Ginzburg O., Larkin S., 2023, *MNRAS*, **522**, 3912
- Chandrasekhar S., 1961, *Hydrodynamic and hydromagnetic stability*
- Codis S., Pogosyan D., Pichon C., 2018, *MNRAS*, **479**, 973
- Danovich M., Dekel A., Hahn O., Teyssier R., 2012, *MNRAS*, **422**, 1732

- Dekel A., Burkert A., 2014, *MNRAS*, 438, 1870
- Dekel A., Devor J., Hetzroni G., 2003, *MNRAS*, 341, 326
- Dekel A., Sari R., Ceverino D., 2009, *ApJ*, 703, 785
- Dekel A., Ginzburg O., Jiang F., Freundlich J., Lapiner S., Ceverino D., Primack J., 2020, *MNRAS*, 493, 4126
- Dekel A., Mandelker N., Bournaud F., Ceverino D., Guo Y., Primack J., 2022, *MNRAS*, 511, 316
- Dekel A., Tziperman O., Sarkar K. C., Ginzburg O., Mandelker N., Ceverino D., Primack J., 2023, *MNRAS*, 521, 4299
- Deriaz E., Perrier V., 2009, *Applied and Computational Harmonic Analysis*, 26, 249
- Dutta Chowdhury D., Dekel A., Mandelker N., Ginzburg O., Genzel R., 2024, *arXiv e-prints*, p. [arXiv:2409.01589](https://arxiv.org/abs/2409.01589)
- Elmegreen B. G., 2011, *ApJ*, 737, 10
- Elmegreen B. G., Burkert A., 2010, *ApJ*, 712, 294
- Farge M., 1992, *Annual Review of Fluid Mechanics*, 24, 395
- Federrath C., Roman-Duval J., Klessen R. S., Schmidt W., Mac Low M. M., 2010, *A&A*, 512, A81
- Fensch J., Bournaud F., 2020, *arXiv e-prints*, p. [arXiv:2011.12966](https://arxiv.org/abs/2011.12966)
- Fisher D. B., et al., 2017, *ApJ*, 839, L5
- Folini D., Walder R., Favre J. M., 2014, *A&A*, 562, A112
- Forbes J. C., et al., 2023, *ApJ*, 948, 107
- Förster Schreiber N. M., et al., 2011, *ApJ*, 739, 45
- Förster Schreiber N. M., et al., 2019, *ApJ*, 875, 21
- Fujimoto S., et al., 2024, *arXiv e-prints*, p. [arXiv:2402.18543](https://arxiv.org/abs/2402.18543)
- Gabor J. M., Bournaud F., 2014, *MNRAS*, 437, L56
- Genzel R., et al., 2008, *ApJ*, 687, 59
- Genzel R., et al., 2011, *ApJ*, 733, 101
- Genzel R., et al., 2014, *ApJ*, 785, 75
- Genzel R., et al., 2023, *ApJ*, 957, 48
- Ginzburg O., Huertas-Company M., Dekel A., Mandelker N., Snyder G., Ceverino D., Primack J., 2021, *MNRAS*, 501, 730
- Ginzburg O., Dekel A., Mandelker N., Krumholz M. R., 2022, *MNRAS*, 513, 6177
- Griv E., Gedalin M., 2012, *MNRAS*, 422, 600
- Guo Y., et al., 2015, *ApJ*, 800, 39
- Guo Y., et al., 2018, *ApJ*, 853, 108
- Hennebelle P., Falgarone E., 2012, *A&A Rev.*, 20, 55
- Hopkins P. F., Christiansen J. L., 2013, *ApJ*, 776, 48
- Hopkins P. F., Quataert E., Murray N., 2012, *MNRAS*, 421, 3488
- Hopkins P. F., Kereš D., Murray N., 2013, *MNRAS*, 432, 2639
- Huertas-Company M., et al., 2020, *MNRAS*, 499, 814
- Immeli A., Samland M., Westera P., Gerhard O., 2004, *ApJ*, 611, 20
- Inoue S., Yoshida N., 2018, *MNRAS*, 474, 3466
- Inoue S., Dekel A., Mandelker N., Ceverino D., Bournaud F., Primack J., 2016, *MNRAS*, 456, 2052
- Jiménez E., Lagos C. d. P., Ludlow A. D., Wisnioski E., 2023, *MNRAS*, 524, 4346
- Kalita B. S., Silverman J. D., Daddi E., Bottrell C., Ho L. C., Ding X., Yang L., 2024, *ApJ*, 960, 25
- Kassin S. A., et al., 2012, *ApJ*, 758, 106
- Kida S., Orszag S. A., 1990, *Journal of Scientific Computing*, 5, 85
- Klessen R. S., Hennebelle P., 2010, *A&A*, 520, A17
- Kravtsov A. V., Klypin A. A., Khokhlov A. M., 1997, *ApJS*, 111, 73
- Kritsuk A. G., Norman M. L., Padoan P., Wagner R., 2007, *ApJ*, 665, 416
- Krumholz M., Burkert A., 2010, *ApJ*, 724, 895
- Krumholz M. R., Burkert B., Forbes J. C., Crocker R. M., 2018, *MNRAS*, 477, 2716
- Lapiner S., et al., 2023, *MNRAS*, 522, 4515
- Li H., Vogelsberger M., Bryan G. L., Marinacci F., Sales L. V., Torrey P., 2022, *MNRAS*, 514, 265
- Livermore R. C., et al., 2015, *MNRAS*, 450, 1812
- Lovelace R. V. E., Hohlfield R. G., 1978, *ApJ*, 221, 51
- Mandelker N., Dekel A., Ceverino D., DeGraf C., Guo Y., Primack J., 2017, *MNRAS*, 464, 635
- Mandelker N., van Dokkum P. G., Brodie J. P., van den Bosch F. C., Ceverino D., 2018, *ApJ*, 861, 148
- Mandelker N., Nagai D., Aung H., Dekel A., Birnboim Y., van den Bosch F. C., 2020, *MNRAS*, 494, 2641
- Mandelker N., Ginzburg O., Dekel A., Bournaud F., Krumholz M. R., Ceverino D., Primack J., 2024, *arXiv e-prints*, p. [arXiv:2406.07633](https://arxiv.org/abs/2406.07633)
- Mayer L., Tamburello V., Lupi A., Keller B., Wadsley J., Madau P., 2016, *ApJ*, 830, L13
- Meng X., Gnedin O. Y., 2020, *MNRAS*, 494, 1263
- Muratov A. L., Kereš D., Faucher-Giguère C.-A., Hopkins P. F., Quataert E., Murray N., 2015, *MNRAS*, 454, 2691
- Nakazato Y., Ceverino D., Yoshida N., 2024, *arXiv e-prints*, p. [arXiv:2402.08911](https://arxiv.org/abs/2402.08911)
- Noguchi M., 1999, *ApJ*, 514, 77
- Ogiya G., Nagai D., 2022, *MNRAS*, 514, 555
- Oklopčić A., Hopkins P. F., Feldmann R., Kereš D., Faucher-Giguère C.-A., Murray N., 2017, *MNRAS*, 465, 952
- Padoan P., Nordlund Å., 2002, *ApJ*, 576, 870
- Renaud F., Boily C. M., Naab T., Theis C., 2009, *ApJ*, 706, 67
- Renaud F., Bournaud F., Kraljic K., Duc P. A., 2014, *MNRAS*, 442, L33
- Renaud F., Segovia Otero Á., Agertz O., 2022, *MNRAS*, 516, 4922
- Renaud F., Agertz O., Romeo A. B., 2024, *A&A*, 687, A91
- Rowland L. E., et al., 2024, *arXiv e-prints*, p. [arXiv:2405.06025](https://arxiv.org/abs/2405.06025)
- Sattari Z., et al., 2023, *ApJ*, 951, 147
- Shibuya T., Ouchi M., Kubo M., Harikane Y., 2016, *ApJ*, 821, 72
- Swinbank A. M., Smail I., Sobral D., Theuns T., Best P. N., Geach J. E., 2012, *ApJ*, 760, 130
- Toomre A., 1964, *ApJ*, 139, 1217
- Wuyts S., et al., 2012, *ApJ*, 753, 114
- Zanella A., et al., 2019, *MNRAS*, 489, 2792
- Zanella A., et al., 2024, *A&A*, 685, A80
- Zolotov A., et al., 2015, *MNRAS*, 450, 2327

## Appendix A: Correspondence between the local and global decompositions

In this appendix we show that, if the compressive and solenoidal components have proportional power spectra, the correspondence indicated in eq. 10 holds. We start by writing the divergence and curl using the Fourier transform

$$\nabla \times \mathbf{v} = \frac{1}{(2\pi)^{3/2}} \int \mathbf{i}\mathbf{k} \times \tilde{\mathbf{v}}(\mathbf{k}) e^{i\mathbf{k}\cdot\mathbf{r}} d^3\mathbf{k}, \quad (\text{A.1})$$

$$\nabla \cdot \mathbf{v} = \frac{1}{(2\pi)^{3/2}} \int \mathbf{i}\mathbf{k} \cdot \tilde{\mathbf{v}}(\mathbf{k}) e^{i\mathbf{k}\cdot\mathbf{r}} d^3\mathbf{k}, \quad (\text{A.2})$$

where  $\tilde{\mathbf{v}}$  is the Fourier transform of  $\mathbf{v}$ . Using Parseval's identity, we can write

$$\int |\nabla \times \mathbf{v}|^2 d^3\mathbf{r} = \int |\mathbf{k} \times \tilde{\mathbf{v}}|^2 d^3\mathbf{k}, \quad (\text{A.3})$$

$$\int |\nabla \cdot \mathbf{v}|^2 d^3\mathbf{r} = \int |\mathbf{k} \cdot \tilde{\mathbf{v}}|^2 d^3\mathbf{k}. \quad (\text{A.4})$$

Next, we can write  $\tilde{\mathbf{v}} = \tilde{\mathbf{v}}_{\text{comp}} + \tilde{\mathbf{v}}_{\text{sol}}$  (see eq. 2). Notice that  $\tilde{\mathbf{v}}_{\text{comp}} \parallel \mathbf{k}$ , while  $\tilde{\mathbf{v}}_{\text{sol}} \perp \mathbf{k}$ . We can therefore rewrite eqs. A.3 and A.4 as

$$\int |\nabla \times \mathbf{v}|^2 d^3\mathbf{r} = \int |\mathbf{k}|^2 |\tilde{\mathbf{v}}_{\text{sol}}|^2 d^3\mathbf{k}, \quad (\text{A.5})$$

$$\int |\nabla \cdot \mathbf{v}|^2 d^3\mathbf{r} = \int |\mathbf{k}|^2 |\tilde{\mathbf{v}}_{\text{comp}}|^2 d^3\mathbf{k}. \quad (\text{A.6})$$

So far, we have not made any assumption about the statistical nature of the velocity field. Next, we assume that  $|\tilde{\mathbf{v}}_{\text{sol}}|^2 = \alpha |\tilde{\mathbf{v}}_{\text{comp}}|^2$ , where  $\alpha$  is a constant in a homogeneous turbulence. This assumption implies that the driving scale and turbulence cascade of both the compressive and solenoidal components are the same. We can therefore write

$$\frac{\int |\nabla \cdot \mathbf{v}|^2 d^3\mathbf{r}}{\int |\nabla \times \mathbf{v}|^2 d^3\mathbf{r} + \int |\nabla \cdot \mathbf{v}|^2 d^3\mathbf{r}} = \frac{\int |\mathbf{k}|^2 |\tilde{\mathbf{v}}_{\text{comp}}|^2 d^3\mathbf{k}}{\int |\mathbf{k}|^2 |\tilde{\mathbf{v}}_{\text{comp}}|^2 d^3\mathbf{k} + \int |\mathbf{k}|^2 |\tilde{\mathbf{v}}_{\text{sol}}|^2 d^3\mathbf{k}} = \frac{\int |\mathbf{k}|^2 |\tilde{\mathbf{v}}_{\text{comp}}|^2 d^3\mathbf{k}}{\int |\mathbf{k}|^2 |\tilde{\mathbf{v}}_{\text{comp}}|^2 d^3\mathbf{k} + \alpha \int |\mathbf{k}|^2 |\tilde{\mathbf{v}}_{\text{comp}}|^2 d^3\mathbf{k}} = \frac{1}{1 + \alpha}. \quad (\text{A.7})$$

Furthermore, again exploiting Parseval's theorem,

$$\frac{\int |\mathbf{v}_{\text{comp}}|^2 d^3\mathbf{r}}{\int |\mathbf{v}|^2 d^3\mathbf{r}} = \frac{\int |\tilde{\mathbf{v}}_{\text{comp}}|^2 d^3\mathbf{k}}{\int |\tilde{\mathbf{v}}_{\text{comp}}|^2 d^3\mathbf{k} + \int |\tilde{\mathbf{v}}_{\text{sol}}|^2 d^3\mathbf{k}} = \frac{\int |\tilde{\mathbf{v}}_{\text{comp}}|^2 d^3\mathbf{k}}{\int |\tilde{\mathbf{v}}_{\text{comp}}|^2 d^3\mathbf{k} + \alpha \int |\tilde{\mathbf{v}}_{\text{comp}}|^2 d^3\mathbf{k}} = \frac{1}{1 + \alpha}. \quad (\text{A.8})$$

We can therefore see that the equality of eq. 10 holds.

## Appendix B: Viscous dissipation decomposition

The viscous dissipation rate per unit volume of a compressible fluid is given by (Chandrasekhar 1961)

$$\Phi = 2\mu \left( e_{ij} e_{ij} - \frac{1}{3} (e_{ii})^2 \right) \quad (\text{B.1})$$

where  $\mu$  is the dynamic viscosity,  $e_{ij} = 1/2(\partial v_i/\partial r_j + \partial v_j/\partial r_i)$ , and we have employed the summation notation. We notice that, since repeated indices are summed over,

$$e_{ij} e_{ij} = \frac{1}{4} \left( \frac{\partial v_i}{\partial r_j} \frac{\partial v_i}{\partial r_j} + \frac{\partial v_j}{\partial r_i} \frac{\partial v_j}{\partial r_i} + 2 \frac{\partial v_i}{\partial r_j} \frac{\partial v_j}{\partial r_i} \right) = \frac{1}{2} \left( \frac{\partial v_i}{\partial r_j} \frac{\partial v_i}{\partial r_j} + \frac{\partial v_i}{\partial r_j} \frac{\partial v_j}{\partial r_i} \right). \quad (\text{B.2})$$

Furthermore,

$$\begin{aligned} |\nabla \times \mathbf{v}|^2 &= \epsilon_{kij} \frac{\partial v_j}{\partial r_i} \epsilon_{klm} \frac{\partial v_m}{\partial r_l} = (\delta_{il} \delta_{jm} - \delta_{im} \delta_{jl}) \frac{\partial v_i}{\partial r_j} \frac{\partial v_l}{\partial r_m} \\ &= \frac{\partial v_i}{\partial r_j} \frac{\partial v_i}{\partial r_j} - \frac{\partial v_i}{\partial r_j} \frac{\partial v_j}{\partial r_i}. \end{aligned} \quad (\text{B.3})$$

Here,  $\epsilon_{kij}$  is the Levi-Civita symbol and  $\delta_{ij}$  is the Kronecker delta. Plugging into eq. B.2, we get

$$e_{ij} e_{ij} = \frac{1}{2} \left( |\nabla \times \mathbf{v}|^2 + 2 \frac{\partial v_i}{\partial r_j} \frac{\partial v_j}{\partial r_i} \right). \quad (\text{B.4})$$

Next, we write

$$\frac{\partial v_i}{\partial r_j} \frac{\partial v_j}{\partial r_i} = \frac{\partial v_i}{\partial r_j} \frac{\partial v_j}{\partial r_i} - \frac{\partial v_i}{\partial r_i} \frac{\partial v_j}{\partial r_j} + \frac{\partial v_i}{\partial r_i} \frac{\partial v_j}{\partial r_j} = \frac{\partial v_i}{\partial r_j} \frac{\partial v_j}{\partial r_i} - \frac{\partial v_i}{\partial r_i} \frac{\partial v_j}{\partial r_j} + (e_{ii})^2. \quad (\text{B.5})$$

Using the product rule,

$$\frac{\partial v_i}{\partial r_j} \frac{\partial v_j}{\partial r_i} = \frac{\partial}{\partial r_j} \left( v_i \frac{\partial v_j}{\partial r_i} \right) - v_i \frac{\partial^2 v_j}{\partial r_j \partial r_i},$$

$$\frac{\partial v_i}{\partial r_i} \frac{\partial v_j}{\partial r_j} = \frac{\partial}{\partial r_j} \left( v_j \frac{\partial v_i}{\partial r_i} \right) - v_j \frac{\partial^2 v_i}{\partial r_i \partial r_j}.$$

Subtracting, as in eq. B.5, and by changing  $i \leftrightarrow j$  in the second term on the right hand side of the second line, we get

$$\frac{\partial v_i}{\partial r_j} \frac{\partial v_j}{\partial r_i} - \frac{\partial v_i}{\partial r_i} \frac{\partial v_j}{\partial r_j} = \frac{\partial}{\partial r_j} \left( v_i \frac{\partial v_j}{\partial r_i} - v_j \frac{\partial v_i}{\partial r_i} \right). \quad (\text{B.6})$$

Plugging this into B.5, and then to B.4, we get

$$e_{ij} e_{ij} = \frac{1}{2} \left( |\nabla \times \mathbf{v}|^2 + \nabla \cdot \left( \overleftrightarrow{D} \mathbf{v} \right) + 2(e_{ii})^2 \right), \quad (\text{B.7})$$

where we have defined  $D_{ij} = 2\partial v_j/\partial r_i - 2(\nabla \cdot \mathbf{v}) \delta_{ij}$ . Wrapping everything back to eq. B.1, we get

$$\Phi = \mu |\nabla \times \mathbf{v}|^2 + \frac{4}{3} \mu (\nabla \cdot \mathbf{v})^2 + \mu \nabla \cdot \left( \overleftrightarrow{D} \mathbf{v} \right) \quad (\text{B.8})$$

Thus, the total viscous dissipation rate in a given volume  $V$ , is

$$\epsilon = \int \Phi d^3\mathbf{r} = \mu \int \left( |\nabla \times \mathbf{v}|^2 + \frac{4}{3} (\nabla \cdot \mathbf{v})^2 \right) d^3\mathbf{r} + \mu \int \left( \overleftrightarrow{D} \mathbf{v} \right) \cdot d^2\mathbf{r},$$



(B.9)

where we have used the divergence theorem to turn the volume integral of  $\nabla \cdot (\overleftrightarrow{D} \mathbf{v})$  into a surface integral. From eq. B.9, we learn that the viscous dissipation rate, and hence the turbulence dissipation rate, is affected by the curl and the divergence of the velocity field inside the volume (Kida & Orszag 1990), but also from a surface term. This surface term vanishes only for specific boundary conditions, like periodic and vanishing at infinity. In these cases, if one thinks of the viscous dissipation rate as the energy injection rate to turbulence, one can qualitatively expect that the total energy in compressive modes of turbulence is  $\propto |\nabla \cdot \mathbf{v}|^2$ , and the total energy in solenoidal modes is  $\propto |\nabla \times \mathbf{v}|^2$ .